

Article

Aging Mechanism of Mn-Based Prussian Blue Cathode Material by Synchrotron 2D X-ray Fluorescence

Mariam Maisuradze ¹, Min Li ¹, Ilaria Carlonagno ², Mattia Gaboardi ², Giuliana Aquilanti ², Jasper Rikkert Plaisier ² and Marco Giorgetti ^{1,*}

¹ Department of Industrial Chemistry “Toso Montanari”, University of Bologna, Campus Navile, Via Piero Gobetti 85, 40139 Bologna, Italy; mariam.maisuradze3@unibo.it (M.M.); min.li2@unibo.it (M.L.)

² Elettra Sincrotrone Trieste, S.S. 14, km 163.5, 34149 Trieste, Italy; ilaria.carlonagno@elettra.eu (I.C.); giuliana.aquilanti@elettra.eu (G.A.); jasper.plaisier@elettra.eu (J.R.P.)

* Correspondence: marco.giorgetti@unibo.it; Tel.: +39-051-2093-666

Abstract: The aging mechanism of 10% and 30% nickel-substituted manganese hexacyanoferrate cathode material in aqueous zinc-ion batteries has been explored through the advanced synchrotron-based two-dimensional X-ray fluorescence technique. Thanks to the two-dimension modality, not only were the metal concentration dynamics throughout the entire electrodes followed during the aging process, but their spatial distribution was also revealed, suggesting the route of the material transformation. The dissolution of Mn and Ni, as well as the penetration of Zn inside the framework were detected, while the Mn aggregations were found outside the hexacyanoferrate framework. Additionally, the possibility of conducting X-ray absorption spectroscopy measurements on the regions of interest made it possible to explore the chemical state of each metal, and furthermore, synchrotron-based powder X-ray diffraction demonstrated the gradual structural modification in 30% Ni-containing sample series in terms of the different phase formation.

Keywords: nickel-substituted manganese hexacyanoferrate; two-dimensional X-ray fluorescence; X-ray absorption near edge structure; X-ray diffraction; zinc-ion batteries; aqueous batteries; double-metal hexacyanoferrate



Citation: Maisuradze, M.; Li, M.; Carlonagno, I.; Gaboardi, M.; Aquilanti, G.; Plaisier, J.R.; Giorgetti, M. Aging Mechanism of Mn-Based Prussian Blue Cathode Material by Synchrotron 2D X-ray Fluorescence. *Batteries* **2024**, *10*, 123. <https://doi.org/10.3390/batteries10040123>

Academic Editor: Yong-Joon Park

Received: 16 March 2024

Revised: 30 March 2024

Accepted: 2 April 2024

Published: 5 April 2024



Copyright: © 2024 by the authors. Licensee MDPI, Basel, Switzerland. This article is an open access article distributed under the terms and conditions of the Creative Commons Attribution (CC BY) license (<https://creativecommons.org/licenses/by/4.0/>).

1. Introduction

Battery material research is a flourishing, yet challenging field in modern-day science. On one hand, energy consumption is constantly increasing, which creates better performance requirement for future developments, but on the other hand, the environmental impact cannot be ignored. Indeed, the European climate law is set for EU to become climate neutral by 2050, including reducing the net greenhouse gas emissions by at least 55% by 2030, compared to 1990 levels [1]. This sets the necessity of making improvements and innovations in both alternative energy sources and their storage fields. Therefore undoubtedly, secondary, or rechargeable, batteries have a great importance, and are widely researched. Even though Li-ion batteries (LIBs) are still dominating in the rechargeable battery market, both environmental and political issues have created the necessity to shift attention mainly in two different directions: the recovery and even reuse of various components in LIBs, and the development of new post-LIB systems.

Development of new systems always requires extensive research. In the battery field, every component of the cell has to be designed, tested, possible problems identified, optimized, and tested again in a cycle until either satisfactory results are reached or the reason behind the failure is identified. For this purpose, advanced structural characterization of the materials is necessary, and X-ray techniques can be considered as one of the best options. For example, X-ray fluorescence spectroscopy (XRF) is a powerful analytical tool for the spectrochemical determination of almost all elements ($Z > 8$). It is based on the measurement of wavelength or energy, and the intensity of the characteristic photons that had

been emitted from the sample, in order to identify the elements inside the analyte and to determine their mass or concentration [2]. Therefore, it can quantifiably provide data about the elemental composition of the material, and consequently, the dynamics of each metal inside the cathode can be tracked. Additionally, with a two-dimensional setup, especially in synchrotron facilities where high spatial resolution is available, elemental distribution throughout the sample can be investigated. This feature is particularly beneficial in the aging studies of battery materials. Moreover, in synchrotron facilities, at the beamlines dedicated to XRF analysis, there is a possibility to record the X-ray absorption spectra (XAS), especially the near-edge portion (XANES) on the regions of interest (micro-XANES experiment), which leads to the development of the tandem characterization technique, covering the determination of the oxidation state of the elements with XAS, while XRF provides the structural information, distribution [3,4], or morphological changes inside the material [5].

Powder X-ray diffraction (PXRD) is another essential tool for probing the long-range structure of material, describing the crystallinity, symmetry, unit cell parameters, and phase modification, that can be extremely helpful for the characterization of battery materials, and for following the alterations inside the structure during the aging process [6].

Even though the research of new battery systems is proceeding with ongoing challenges, progress is still being achieved. Indeed, the commercialization of the first Na-ion batteries (SIBs) by Contemporary Amperex Technology Co., Ltd., Ningde, Fujian, China, in 2021, could be counted as a big step. Their cathode material is based on the Prussian White, from the family of the Prussian Blue Analogues (PBAs) [7]. Interestingly, the other prototypes of SIBs, also based on PBAs, are being developed in Sweden [8] and USA [9]. Alongside SIBs, other post-LIBs are also being extensively researched, including potassium, calcium, magnesium, zinc, etc. The latter is attractive not only as a low cost, nontoxic material, but also, in case of using Zn metal as an anode [10–12], its high theoretical gravimetric (820 mAh g^{-1}) and volumetric capacity (5855 mAh cm^{-3}), and low standard reduction potential (-0.76 V vs. SHE) [11] can be certainly counted as advantages.

Indeed, the family of PBAs is highly promising in the battery field, as their open ionic channels lead to the higher diffusion coefficient of 10^{-9} to $10^{-8} \text{ cm}^2 \text{ s}^{-1}$ [13,14], and therefore to higher ionic conductivity. Also, the structural and dimensional stability of a PBA lattice, originating from its robust and large 3D channel frameworks, leads to almost zero lattice strain towards the insertion and extraction processes [15,16]. The general formula of PBAs can be written as: $A_xM^1[M^2(CN)_6]_{\gamma}\square_{1-\gamma}\cdot zH_2O$, where A is an alkali metal such as Li^+ , Na^+ , K^+ , etc.; M^1 and M^2 are transition metal ions (Fe, Co, Mn, Ni, Cu, etc.); \square is a vacancy; $0 < x < 2$; $0 < y < 1$ [16]. Generally, both metals (M^1 and M^2) can be partially or fully substituted with various other transition metals, making this family of materials extremely tunable. Also, both metal centers can be (but are not necessarily) electroactive, which implies they have two electron redox capacity, and therefore two alkali ion storage. Various PBAs have been reported as electrode materials for both Li-ion and post-Li-ion battery systems [17–24].

Manganese hexacyanoferrate (MnHCF) is one of the simple PBAs, with attractive qualities such as safety and nontoxicity, but also, due to containing only elements which are widely abundant, it is relatively inexpensive and sustainable [6]. In the battery field, MnHCF is promising as a cathode material, as it possesses relatively high discharge voltage and two active redox couples ($\text{Fe}^{3+}/\text{Fe}^{2+}$ and $\text{Mn}^{3+}/\text{Mn}^{2+}$), leading to the large specific capacity. However, Mn in an oxidized +3 state is subjected to the severe crystal Jahn-Teller (JT) distortion effect [25,26], which is believed to be one of the reasons for the serious dissolution of MnHCF in aqueous zinc-ion batteries (AZIBs), forming a new Zn-containing phase [27–29]. Therefore, capacity decrease is an issue for this system and different strategies have been utilized to solve it. Table S1 shows several reported values of capacity and stability of MnHCF in AZIBs. Heteroatom doping or partial substitution approaches are sometimes successfully adopted for the adjustment of the electrochemical properties of MnHCF. It is reported that Ni doping can help to relax the JT distortion in

MnHCF [30], as Ni and Mn have a similar atomic radius, and therefore, the framework remains in a good order during the substitution. Notably, Ni sites are believed to be unreactive during the insertion/extraction process, and just balance the tiny structural disturbances originating from the redox reactions on the Mn sites [31]. The synthesis, as well as the IR and the XRPD characterization of 10% and 30% Ni-substituted MnHCF powder has been reported previously [32].

During the cycling process, the structure and/or morphology of the electrode material can undergo some modification, which needs thorough investigation for the proper understanding of the aging mechanism of the battery. Microscopical techniques are extremely useful for morphological characterization, while the structure can be explored through spectroscopic techniques. SEM or HR-TEM coupled with XRD, XPS, EELS, EDS, etc. have been reported in various different studies [33,34]. In this work, we followed the structural and morphological modification during the aging process of 10% and 30% Ni-substituted MnHCF (10%NiMnHCF and 30%NiMnHCF, respectively) cathode materials from AZIBs with synchrotron-based 2D-XRF, with additional XANES measurements on the regions of interest and PXRD. The application of these characterization techniques can be generalized for the various different compounds in a number of fields, including other battery system researches.

2. Materials and Methods

2.1. Synthesis

The synthesis of NiMnHCF was performed through simple and scalable co-precipitation method [26,32]. Manganese sulphate monohydrate ($\text{MnSO}_4 \cdot \text{H}_2\text{O}$), nickel sulphate (NiSO_4), sodium ferrocyanide decahydrate ($\text{Na}_4[\text{Fe}(\text{CN})_6] \cdot 10\text{H}_2\text{O}$), and sodium sulphate (Na_2SO_4) were utilized without further purification (Sigma Aldrich). For obtaining the 10% and 30% concentration of nickel, the aqueous solutions of $\text{MnSO}_4 \cdot \text{H}_2\text{O}$ and NiSO_4 were preliminarily mixed in 90/10 and 70/30 ratios, respectively. Afterwards, these mixtures, together with the aqueous solution of $\text{Na}_4[\text{Fe}(\text{CN})_6] \cdot 10\text{H}_2\text{O}$, were added dropwise to an aqueous solution of Na_2SO_4 (0.1 L, of each 0.1000 M solution). A peristaltic pump was set at a rate of 3.3 mL min^{-1} , under continuous magnetic stirring and constant temperature (with a thermostatic bath, temperature: $40 \pm 2^\circ\text{C}$). The obtained products were aged for 5 days, centrifugated, and the solid fraction washed three times with the distilled water. Powders were dried at 60°C for 48 h, and ground in an agate mortar. Microwave plasma atomic emission spectroscopy (MP-AES), which was performed on an MP-AES 4210 high sensitivity optical emission spectrometer, and thermogravimetric analysis (TGA), which was carried out on a TA Discovery TGA instrument, were applied to the synthesized materials. The obtained formulas were: $\text{Na}_{1.4}\text{Mn}_{0.90}\text{Ni}_{0.10}[\text{Fe}(\text{CN})_6]_{0.76} \cdot 3.4\text{H}_2\text{O}$ and $\text{Na}_{1.52}\text{Mn}_{0.68}\text{Ni}_{0.32}[\text{Fe}(\text{CN})_6]_{0.76} \cdot 3.53\text{H}_2\text{O}$.

2.2. Electrode Preparation

Dried samples were mixed with a conductive agent (carbon black) and a binder (polytetrafluoroethylene (PTFE)) in a mortar, with a ratio of 70:25:5. Electrodes were cut, with a size of 8 mm and 12 mm in diameter, and a mass loading of approximately $8 \pm 1 \text{ mg}_{\text{NiMnHCF}} \text{ cm}^{-2}$. A two-hour long soaking of the pellets in the electrolyte solution under vacuum was applied before the electrochemical tests. Coin cells were assembled with NiMnHCF as the cathode, Zn metal plate as the anode, 3M ZnSO_4 aqueous solution as an electrolyte, and Whatman paper as a separator. The tests of the galvanostatic cycling with potential limitation (GCPL) were performed with the conditions of $1 < E < 1.85 \text{ V}$ versus Zn^{2+}/Zn , with a scan rate of 20 mA g^{-1} on a Neware BTS4000-5V100mA battery testing system.

2.3. 2D-XRF and XANES Setup

The data were collected at the XRF beamline in Sincrotrone Elettra, Basovizza, Italy. This beamline hosts an end station dedicated to spectrometry, spectroscopy, microscopy,

and reflectometry [35]. A double crystal Si(111) monochromator with $\Delta E/E \approx 10^{-4}$ enables access to the energy range of 4–14 keV [36]. The beam size was set through two pairs of exit slits; the horizontal and vertical apertures were 100 μm and 200 μm , respectively. Considering the 45°/45° geometry used in our experiment, the beam footprint on the sample surface was 140 × 200 μm^2 (H × V).

In the experiments dedicated to ex situ electrodes from AZIBs, because of the composition of the materials, an initial energy of 10 KeV was chosen (above Mn, Fe, Ni, and Zn K-edges). For the data analysis of XRF maps and spectra, PyMca 5.8.0 software was used [37]. XRF spectra can be extracted from every single pixel of the recorded maps. The spectra were calibrated and normalized to the beam intensity and, when areas including multiple pixels were selected and considered, the resulting spectra were also normalized to the number of pixels in the selection. For the semi-quantitative analysis representative of the entire electrodes, sample areas were selected from the corresponding maps, avoiding the visible morphological defects or heterogeneities. The spectra were subsequently fitted using the same software. The elemental composition at the heterogeneities was quantified in the same manner, obtaining the elemental concentrations as mass fractions.

XAS measurement was performed on several samples, in selected areas, in fluorescence mode. The data analysis of XANES spectra was performed with Athena software (Demeter 0.9.26) [38].

The list of the ex situ electrodes is reported in Table 1.

Table 1. List of samples analyzed with 2D-XRF and micro-XANES experiments.

Samples	Description	2D-XRF		XANES	
		10%NiMnHCF	30%NiMnHCF	10%NiMnHCF	30%NiMnHCF
Pristine	Fresh electrode	✓	✓	✓	✓
C1	Charged after 1st cycle	✓	✓	✓	✓
D1	Discharged after 1st cycle	✓	✓	✓	-
C2	Charged after 2nd cycle	✓	✓	✓	-
D2	Discharged after 2nd cycle	✓	✓	✓	-
C10	Charged after 10th cycle	✓	✓	-	-
D10	Discharged after 10th cycle	✓	-	-	-
C100	Charged after 100th cycle	✓	✓	-	-

2.4. PXRD Setup

PXRD analysis of 30%NiMnHCF was performed on the MCX beamline at Sincrotrone Elettra, Basovizza, Italy. The monochromatic X-ray beams of 1.03318 Å and 0.62000 Å (for aged samples) were used in the transition mode with a marCCD detector, step size 0.01° and acquisition time of 1 s/step. Samples were attached with paper-tape on the sides, or were embodied in double Kapton tape (in the case of aged electrodes). Background, Kapton tape, and standard LaB₆ were analyzed. The crystal structure was refined by GSAS II [39]; in the following work Q (Å⁻¹) will be used for the x -axis of the diffractograms, instead of 2θ (°), because of the different wavelengths of the X-ray beam between the analyses. The list of samples is presented in Table S2.

3. Results and Discussion

3.1. 2D-XRF and Micro-XANES Analysis

XRF images recorded on the pristine electrodes of both 10% and 30%NiMnHCF shows (Figures 1 and S1, pristine shortened to “Pr”) that the distribution of all framework metals

inside the entire sample is quite homogeneous. The lower intensities near the borderline can be explained by the thinner edges of the handmade pellets.

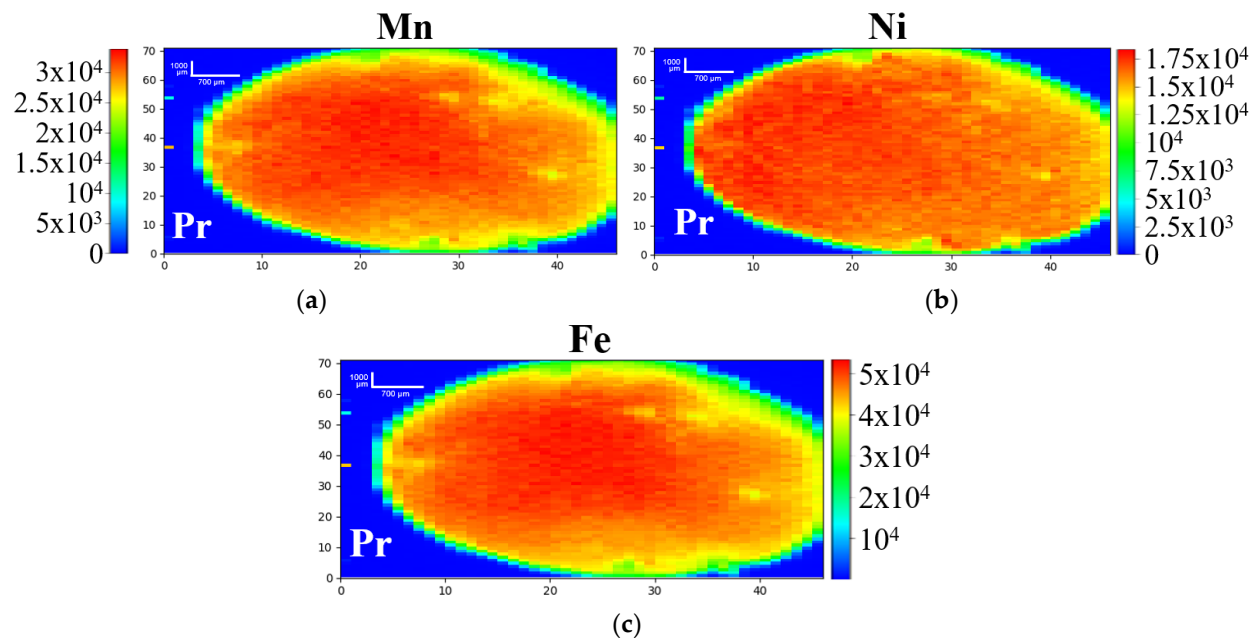


Figure 1. Normalized 2D-XRF maps of 30%NiMnHCF pristine ex situ electrode: (a) Mn, (b) Ni, (c) Fe. Intensity scale is color-based (red = high intensity; blue = low intensity). Length scale: Vertical bar 1000 μm (200 $\mu\text{m} \times 5$ px), horizontal bar 700 μm (140 $\mu\text{m} \times 5$ px).

The 30%NiMnHCF C1 sample shown in Figure 2a demonstrates the dissolution of Mn, which has already been described in the case of pure MnHCF [40]. Evidently, the process starts from the borders. Similarly, Ni (Figure 2b) suffered the partial dissolution, initially also from the edges of the electrode. Therefore, nickel not only failed to stabilize the MnHCF structure in the aqueous zinc media, but by itself was subjected to the dissolution. Zn, on the other hand, is detected inside the framework already in C1 (Figure 2c), even though during the first charge only Na from the synthesis process was expected to leave the structure. Zn was detected throughout the whole sample, but with a higher intensity on the borderline, which possibly indicates the insertion of Zn inside the framework from the borders, occupying the positions of Mn and Ni, as their dissolution exactly started from the edges (Figure 2d). This phenomenon is observed for both 10% and 30% NiMnHCF (see more examples later).

The process deepened in the following cycles; however, by the 10th cycle, the metal distribution in electrodes became homogeneous again. This is well visible on Figure S2, which depicts how the uniform distribution of Ni in 10%NiMnHCF changed to the relatively high residual concentration of Ni only in the center of the samples, and then again became homogeneous. Indeed, the semi-quantitative analysis relative to Fe shows the rapid drop of the concentration of Mn from the pristine electrodes to the C1s, and then a slower decrease until equilibrium is reached (Figure 3a,b). Interestingly, the content of Mn (and Ni) is higher in the charged samples, compared to the discharged ones of the same cycle. This phenomenon indicates that while the big portion of Mn left the structure entirely, there is a small fraction of manganese which is reversibly forced out of the framework when Zn-ions from the electrolyte enter it during the discharge process. This argument is further strengthened by the fact that Zn demonstrates the opposite behavior to Mn and Ni (higher concentrations in discharged electrodes).

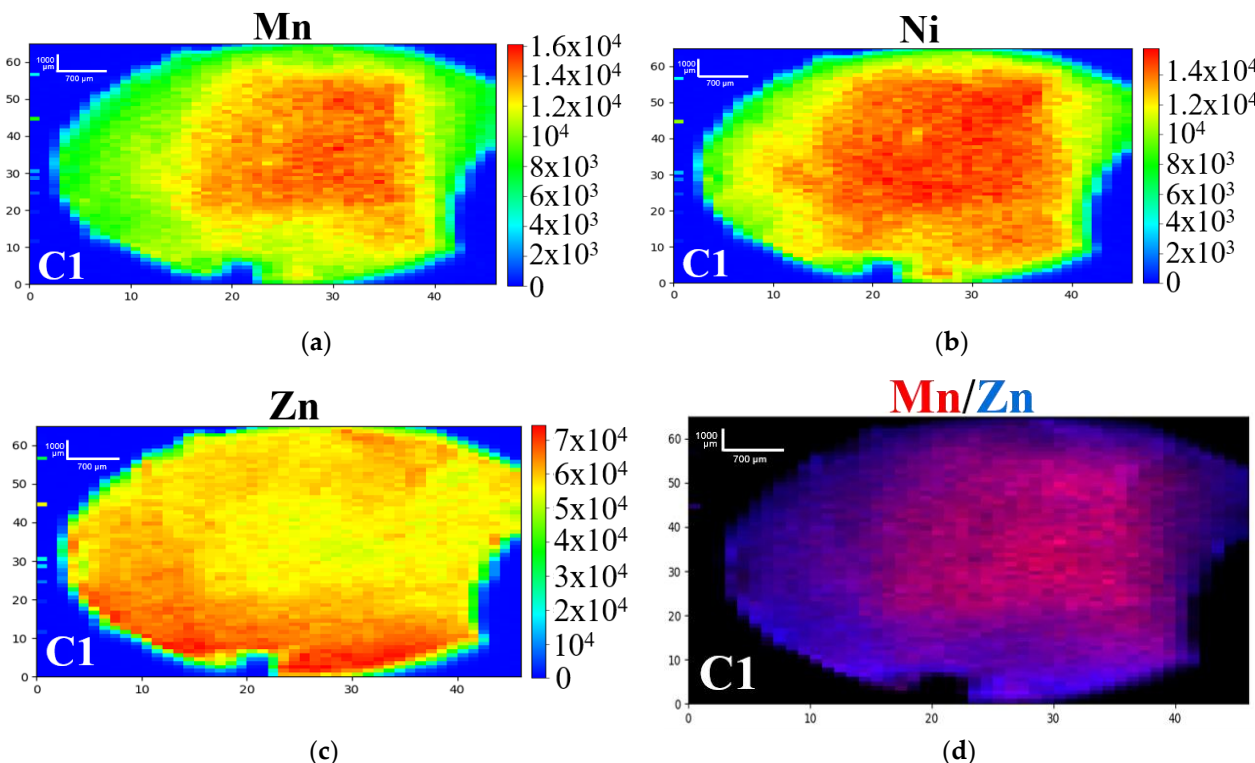


Figure 2. Normalized 2D-XRF maps of 30%NiMnHCF C1 ex situ electrode: (a) Mn, (b) Zn, (c) Ni, (d) Mn and Zn overlay (Mn in red, Zn in blue). For (a–c), intensity scale is color-based (red = high intensity; blue = low intensity). Length scale: Vertical bar 1000 μm (200 $\mu\text{m} \times 5$ px), horizontal bar 700 μm (140 $\mu\text{m} \times 5$ px).

The 10% and 30%NiMnHCF not only have a similar behavior, but more importantly, as Figure 3c–e indicate, during the aging process, the ratios of Mn/Fe, Ni/Fe and Zn/Fe become closely similar already after 10 cycles, indicating that there are no significant differences between 10% and 30%NiMnHCF anymore; essentially, they transform into the same compound.

At the XRF beamline, samples can be investigated using complementary XAS measurements carried out under the same experimental conditions and with the same beam size used for XRF mapping. In this case, it was interesting to explore the extra information about the possible differences in the oxidation state or any modifications in the coordination of the metals between the different portions of the sample. On the XRF images, it is easy to assess the elemental distribution within the pellet; therefore, several points were chosen to investigate the behavior of metals in areas where their concentration largely differs from the average.

Figure S3 shows the Fe, Mn, and Ni K-edge spectra of the pristine electrode and Zn K-edge spectrum of C1 of 10%NiMnHCF, recorded on small sections of the pellets. XAS spectra of the initial framework metals share the features, which have been already recorded on powder samples [32], while the Zn spectrum possesses the characteristics of ZnHCF, being in a good agreement with the previous reports [40]. Much more meaningful is the XANES recorded on the portions where the sample looks inhomogeneous. Indeed, the measurement was performed on a small aggregate of Mn (marked with a blue circle), which was formed in C1 sample of 10%NiMnHCF (Figure 4a,b), where the concentration of Mn exceeded the average value approximately 1.5 times. The spectral decline from the hexacyanoferrate pattern was evident (Figure 4c). Linear combination fitting (LCF) was adopted to shed some light about this modification. As Figure 4d shows, the main component of the fit is MnO_2 , which consists of more than 60% of the total contribution

(Table 2). Therefore, the formation of the Mn(IV) oxide starts non-uniformly throughout the electrode.

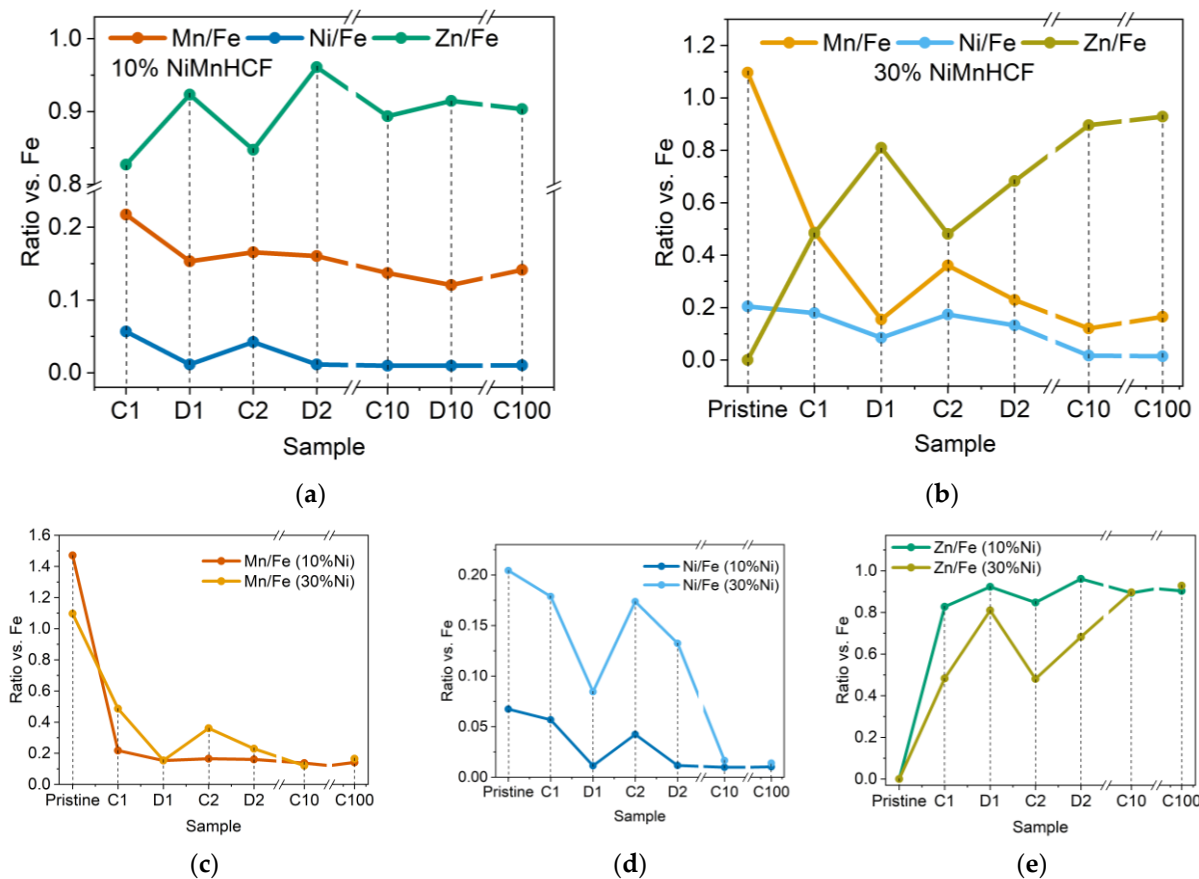


Figure 3. 2D-XRF semi-quantitative analysis results showing the dynamics of Mn, Ni, and Zn vs. Fe in ex situ electrodes for the (a) 10%NiMnHCF series and the (b) 30%NiMnHCF series. The dynamics of (c) Mn vs. Fe, (d) Ni vs. Fe, and (e) Zn vs. Fe in the NiMnHCF electrodes.

Table 2. The LCF results of Mn K-edge of 10%NiMnHCF C1 cathode hotspot with components: pristine, MnSO_4 , MnO , Mn_3O_4 , Mn_2O_3 , and MnO_2 .

	Pristine	MnSO_4	MnO	Mn_3O_4	Mn_2O_3	MnO_2	R-Factor	Reduced χ^2
Ratio	0.159	0.148	0.001	0	0.089	0.604		
Error	0.028	0.017	0.024	0.032	0.068	0.028	0.00255	0.00059

Predictably, the Mn aggregates are more frequent in the aged electrodes. As mentioned above, the C10 samples look quite homogeneous, so the dissolution of Mn (Ni), and its substitution with Zn seems to have reached the equilibrium (or a near equilibrium state). However, in the C10 and C100 samples, close to the edges and near the defects of the electrodes, there appears to be a few Mn aggregations, and interestingly, these regions lack other framework atoms (Figures 5 and S4). According to the semi-quantitative analysis, the concentration of manganese in these aggregates, for example, inside the 30%NiMnHCF C100, is more than four times higher to the average content of Mn. Possibly, the portion of dissolved Mn formed small aggregates of oxide species outside the hexacyanoferate structure (similarly to what was singularly visible in C1 of 10%NiMnHCF).

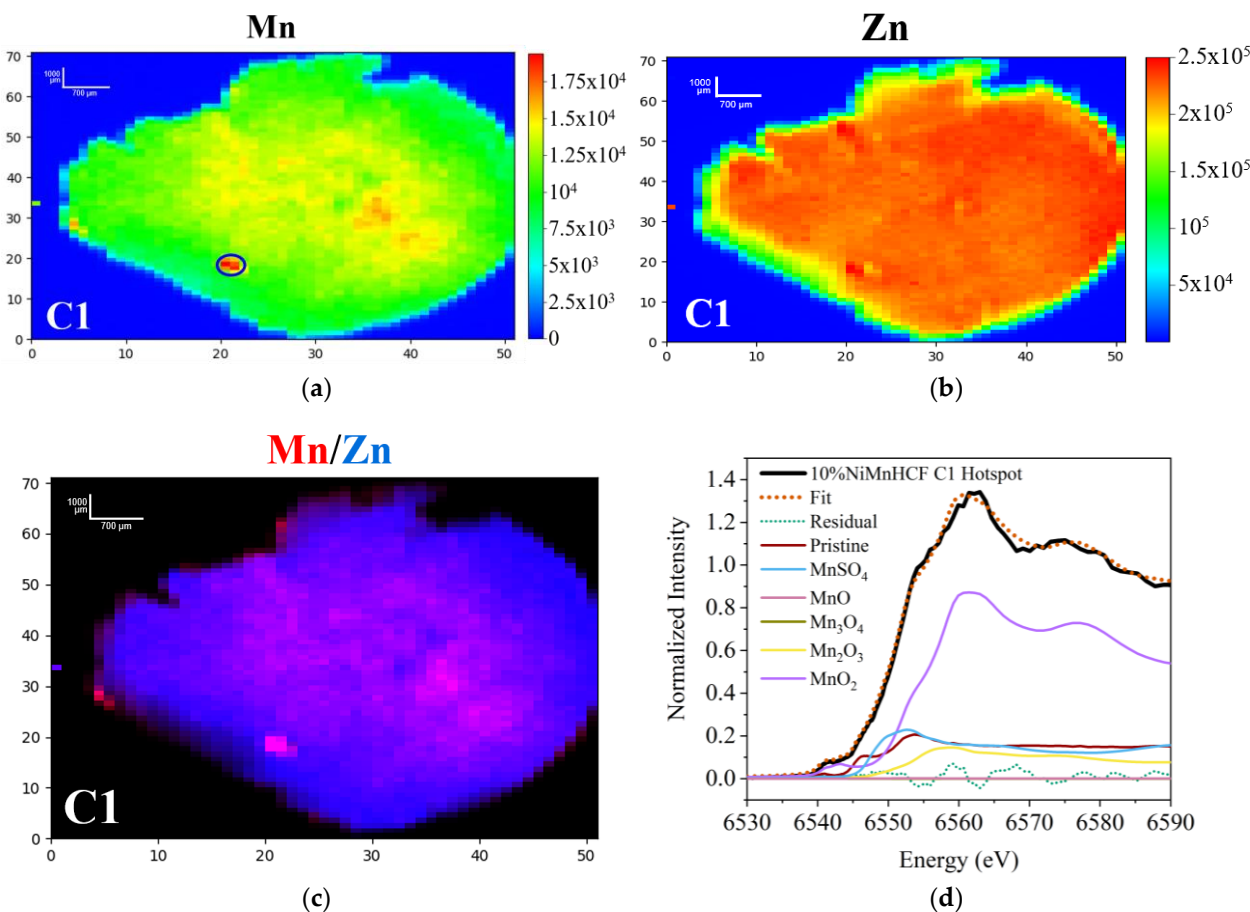


Figure 4. Normalized 2D-XRF maps of 10%NiMnHCF C1 ex situ electrode. (a) Mn, inhomogeneity marked with a blue circle; (b) Zn, intensity scale is color-based (red = high intensity; blue = low intensity); (c) Mn and Zn overlay (Mn in red, Zn in blue). Length scale: Vertical bar 1000 μm ($200 \mu\text{m} \times 5 \text{ px}$), horizontal bar 700 μm ($140 \mu\text{m} \times 5 \text{ px}$); (d) LCF analysis of the XANES spectrum of C1 hotspot, components: pristine, MnSO_4 , MnO , Mn_3O_4 , Mn_2O_3 , MnO_2 .

To further confirm the existence of the two compounds: ZnHCF and MnO_2 inside the NiMnHCF material, electrochemical and other material characterization methods have been deployed.

3.2. IR Analysis

The IR spectra of both NiMnHCF compounds have already been reported previously [32]. The signal of $\text{C}\equiv\text{N}$ stretching was centered at 2074 and 2077 cm^{-1} for 10%NiMnHCF and 30%NiMnHCF, respectively, which also was in agreement with the results of pure MnHCF, as reported in the literature [40]. As Figure 6a,b show, for the pristine electrodes, only a slight shift of $\text{C}\equiv\text{N}$ stretching is visible to 2067–2069 cm^{-1} . But in the cycled electrodes the obvious blue shift of 32–33 cm^{-1} was observed. These values are much closer to $\text{C}\equiv\text{N}$ stretching for ZnHCF material, for which the value of approximately 2100 cm^{-1} has been reported [41]. This observation strengthens the argument of tandem 2D-XRF–micro-XANES analysis, which indicated Zn penetration inside the sample through the obtained maps, and suggested ZnHCF formation through the recorded XANES spectra (Figures 3 and S3).

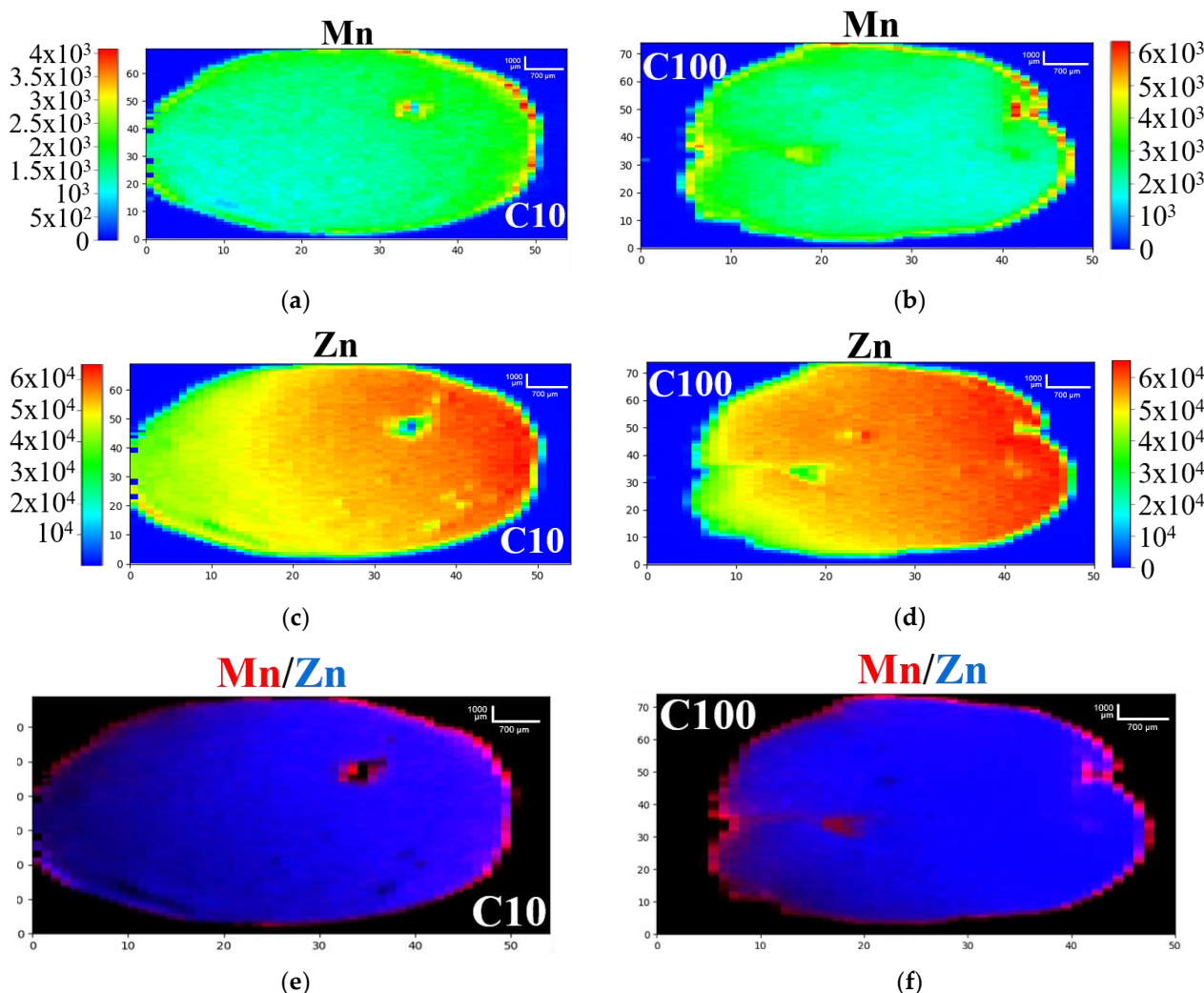


Figure 5. Normalized 2D-XRF maps of 30%NiMnHCF ex situ electrode: (a) Mn C10, (b) Mn C100, (c) Zn C10, (d) Zn C100. Intensity scale is color-based (red = high intensity; blue = low intensity). (e) Mn and Zn overlay of C10, (f) Mn and Zn overlay of C100 (Mn in red, Zn in blue). Length scale: Vertical bar 1000 μm (200 $\mu\text{m} \times 5$ px), horizontal bar 700 μm (140 $\mu\text{m} \times 5$ px).

3.3. GCPL Analysis

To cross-examine the formation of MnO_2 in electrodes during the cycling, the electrochemical characterization results can be addressed. Generally, in the first cycle, Na^+ is expected to be leaving the structure while charging, and Zn^{2+} to intercalate during the discharge process. In the later cycles, Zn^{2+} should reversibly enter the NiMnHCF framework; however, as Figure 6c shows, the capacity of 30%NiMnHCF keeps steadily declining up to 15 cycles before the stabilization, more prominently during the initial several cycles, which suggests the presence of an activation phase and/or gradual structural transformation (the same trend is observed for 10%NiMnHCF, Figure S5). This can be due to the observed formation of the manganese oxide, as reported in Section 3.1 (Figures 4 and 5). In the first couple of cycles, the discharge plateaus are slowly forming and stabilizing for both 10% and 30%NiMnHCF at approximately 1.28 V and 1.46 V (V vs. Zn^{2+}/Zn) (Figure 6d). The plateaus at these potentials are indeed characteristic to the MnO_2 cathode material [42], which indicates that, after the formation of the oxide species, it becomes the major contributor of the electrochemical activity of the system. Notably, after the stabilization (10–15 cycles), the discharge capacity is quite stable, and has only slight periodicity (Figures 6c and S5).

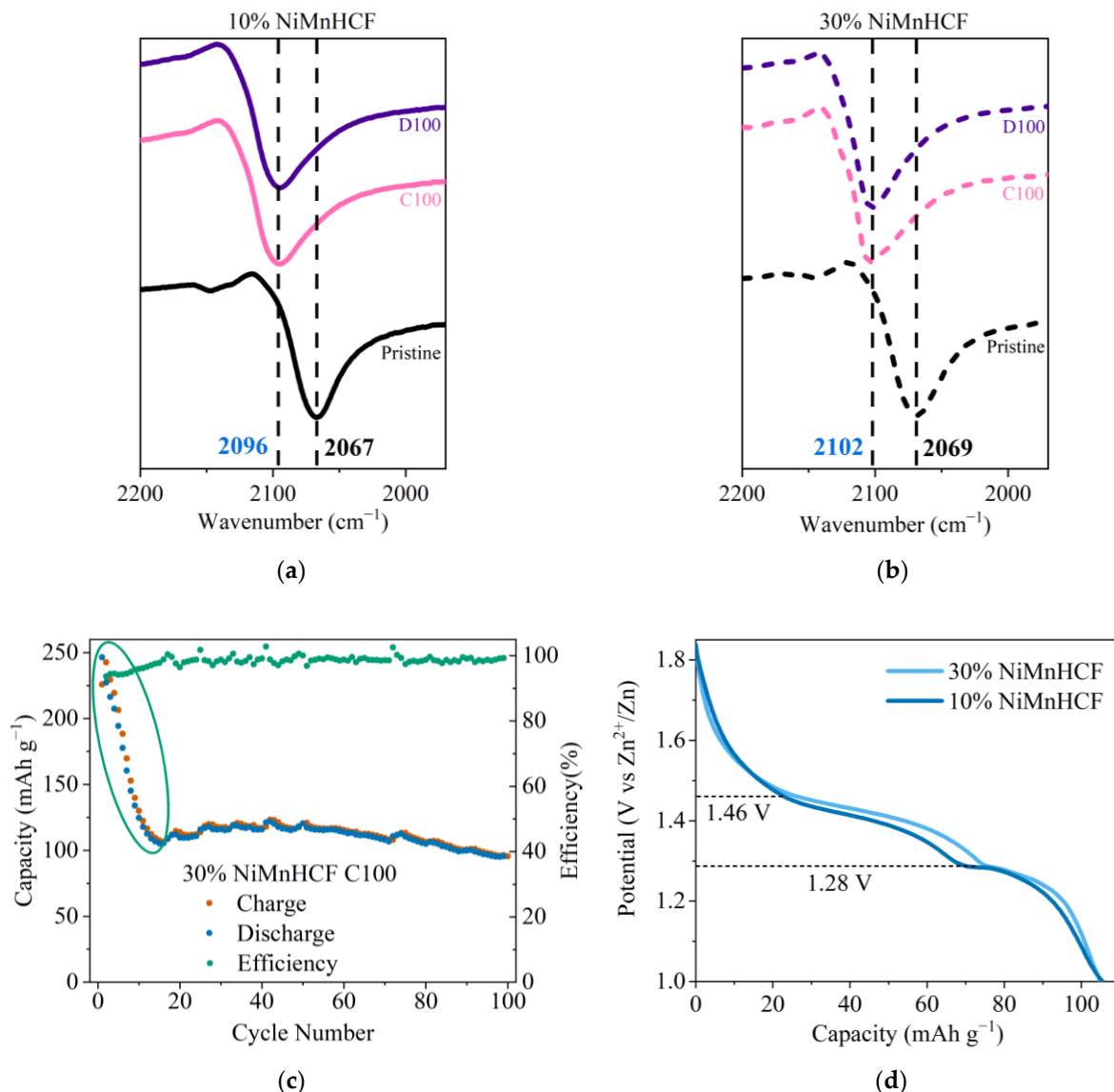


Figure 6. ATR-FT-IR analysis results of pristine and cycled electrodes of (a) 10%NiMnHCF, (b) 30%NiMnHCF; GCPL data of (c) stability and efficiency of the C100 of 30%NiMnHCF, (d) discharge curve after the stabilization of 10% and 30%NiMnHCF (extracted from same cycle).

3.4. PXRD Analysis

Additionally, the pristine sample of 30%NiMnHCF was refined to the face-centered cubic F m-3m space group (Figures 7a and S6), similarly to the as-synthesized powdered sample, which had already been analyzed before [32]. According to the Rietveld refinement results, the unit cell experienced a slight decrease of the cell volume, with the a parameter reduced from $a = 10.4317 \text{ \AA}$ to $a = 10.33 \text{ \AA}$.

The structural modifications started from the first charging process, consisting of not only the modification of the cell parameters or strain inside the system, but the emergence of a new phase. Figure 7b demonstrates that the C1 sample can be characterized as a sum of two phases, the original F m-3m, and a new primitive cubic phase P m-3m with a larger unit cell ($a = 11.82 \text{ \AA}$).

The structural reversibility is a very important aspect for the longer lifetime of the battery systems; in this material, the modifications seem to be non-reversible, as the XRD pattern of D1 structure did not resemble pristine electrode (Figure S7), and was still a mixture of two phases. With further cycling, the transformation continues and the original phase slowly disappears; the C2 and D2 electrodes prove the same observation (Figure S8).

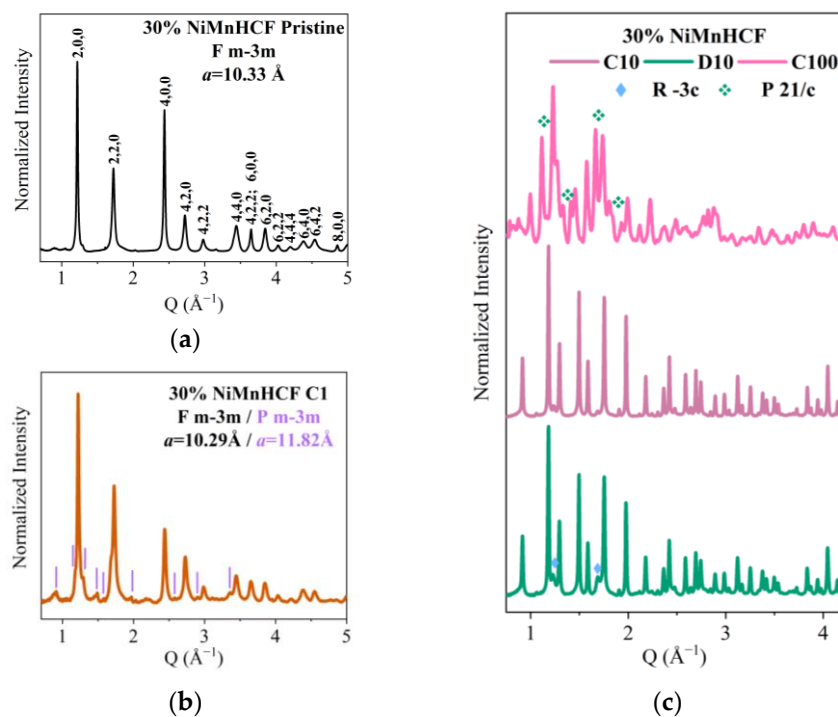


Figure 7. PXRD measurement results of 30%NiMnHCF ex situ electrodes: (a) Pristine, (b) C1, (c) C10, D10, and C100.

The initial F m-3m phase is not visible in the tenth cycle of 30%NiMnHCF samples. As Figure 7c shows, the diffractograms of C10 and D10 are highly crystalline and very similar, indicating the stabilization of the structure. The samples were refined to the P m-3m phase, but the presence of two unindexed low intensity reflections (depicted with blue rhombus) in D10 sample suggested the existence of an additional phase. Because the formation of ZnHCF was already indicated by several techniques, hexagonal R -3c, characteristic to the ZnHCF material [41] was added during the refinement, as a second phase,. Indeed, the low intensity peaks were fitted perfectly (Figure S9).

Two pellets from the 50th cycle also displayed multiple phases inside the structure, and the initial F m-3m was not recovered; instead, the mix of primitive cubic and hexagonal phases were detected, and the compound was still quite crystalline (Figure S10). But when the C100 and D100 were analyzed (Figures 7c and S11), the main phase became the hexagonal R-3c, characteristic to ZnHCF, while the P m-3m cell was still visible inside the 100th cycle samples. Consequently, the part of the primitive cubic cell partially transformed to the hexagonal symmetry. The initial refinement of the 100th cycle samples was performed considering those two phases; however, the fit improved after adding the third phase, coming from the electrolyte, the monoclinic P 21/c unit cell, characteristic of hydrated zinc sulphate ($\text{ZnSO}_4 \cdot 4\text{H}_2\text{O}$). Unfortunately, the data quality was not high enough to retrieve the reliable information about the phase ratio. The crystallinity inside the structure also seemingly decreased.

For better visualization of the overall structure evolution of the cathode material during the aging process, diffractograms were stacked on top of each other (Figure S12). The detailed information about the unit cell parameters of each phase for 30%NiMnHCF can be found in Table 3. The numbers were obtained from the Pawley refinement results (except pristine electrode, where Rietveld refinement was performed, Figures S13–S22).

Overall, PXRD and 2D-XRF results are aligned, as the dissolution of Mn and Ni and the penetration of Zn inside the framework might have caused the formation of the new phase. The fact that the reflections of MnO_2 were not visible in diffractograms can be explained by the possible amorphization and/or not being able to form the long-range

ordered structure, as this compound is known to exist in several different forms, including the amorphous one [43].

Table 3. The cell parameters of different phases, presented in the series of 30%NiMnHCF cathodes.

30%NiMnHCF Samples	Cell Parameters							
	F m-3m		P m-3m		R -3c		P 21/c	
	a (Å)	a (Å)	a (Å)	c (Å)	a (Å)	b (Å)	c (Å)	β (°)
Pristine	10.33	-	-	-	-	-	-	-
C1	10.29	11.82	-	-	-	-	-	-
D1	10.22	11.79	-	-	-	-	-	-
C2	10.33	11.88	-	-	-	-	-	-
D2	10.16	11.76	-	-	-	-	-	-
C10	-	11.91	-	-	-	-	-	-
D10	-	11.88	12.42	32.85	-	-	-	-
C50	-	11.99	12.48	32.94	-	-	-	-
D50	-	12.05	12.46	32.74	-	-	-	-
C100	-	11.94	12.37	33.08	6.23	13.77	9.91	125.45
D100	-	11.99	12.48	32.94	6.16	13.69	9.77	126.84

4. Conclusions

The 2D-XRF measurement showed the spatial distribution of the elements inside the electrode, and the modification of this distribution. XRF maps provided the visual pattern of the dissolution of Mn and Ni, starting from the borders, and Zn entering the structure exactly from the edges. Therefore, Ni was not able to provide stability to the MnHCF structure, as it was hoped. The semi-quantitative measurement showed the dynamics of the elements inside the pellets: Ni and Mn had a lower concentration in the discharged electrodes (compared to the charged ones of the same cycle), while Zn showed the opposite behavior, the equilibrium already being reached by the 10th cycle. Most importantly, compositionally this equilibrium was same for the 10%NiMnHCF and 30%NiMnHCF, as they were proven to contain almost identical metal ratios, effectively becoming the same material.

The XANES measurements suggested Zn to be integrated in the hexacyanoferrate framework from the first cycle. This observation was further strengthened by the PXRD measurements, demonstrating the modification of the material through the phase transformation from the face-centered cubic unit cell to primitive cubic, and then partially to the hexagonal symmetry, generally characteristic to ZnHCF, with the additional monoclinic phase from the electrolyte contribution. The same compound (ZnHCF) formation was suggested by the FT-IR/ATR analysis.

On the other hand, the 2D-XRF maps showed the systematical Mn aggregations on the edges of the aged samples (already in the 10th cycle). With the overlay maps, it was evident that these regions lacked other metals, suggesting Mn to be in a different (i.e., not hexacyanoferrate) form. The XANES spectrum of the Mn hotspot suggested that these aggregations mainly consist of MnO_2 , which was also verified by the electrochemical profile of the material after the stabilization.

Together, these X-ray techniques can provide a thorough understanding of the processes appearing during cycling of the battery system, as the tandem XRF-micro-XANES experiments are able to follow the gradual modification of the materials, and understand the inhomogenization, alteration, or degradation of the electrodes (spatially with XRF images, and chemically with XANES spectra) while the multiphase changes in the long-range order domain are exploratory by the PXRD measurements. The approach presented in this work can be extended to similar studies on anode or other cathode materials to be used in the next generation of battery electrodes.

Supplementary Materials: The following supporting information can be downloaded at: <https://www.mdpi.com/article/10.3390/batteries10040123/s1>, Figure S1: 2D-XRF maps of Pristine sample of 10%NiMnHCF: (a) Mn, (b) Ni, and (c) Fe; Figure S2: 2D-XRF maps of Ni contribution of 10%NiMnHCF samples: (a) Pristine, (b), C1, (c) C2, and (d) C10; Figure S3: XANES of 10%NiMnHCF samples: (a) Mn K-edge of Pristine, (b), Fe K-edge of Pristine, (c) Ni K-edge of Pristine, and (d) Zn K-edge of C1; Figure S4: 2D-XRF maps of 10%NiMnHCF samples: (a) C10 Mn, (b), C100 Mn, (c) C10 Zn, (d) C100 Zn, (e) C10 Mn/Zn overlay, and (f) C100 Mn/Zn overlay; Figure S5: GCPL data of C100 of 10%NiMnHCF: stability and efficiency test; Figure S6: F m-3m structure of 30%NiMnHCF; Figure S7: PXRD measurement result of D1 of 30%NiMnHCF; Figure S8: PXRD measurement results of C2 and D2 of 30%NiMnHCF; Figure S9: Pawley refinement of D10 of 30%NiMnHCF; Figure S10: PXRD measurement results of C50 and D50 of 30%NiMnHCF; Figure S11: PXRD measurement result of D100 of 30%NiMnHCF; Figure S12: PXRD measurement result of D100 of 30%NiMnHCF; Figure S13: Rietveld refinement of Pristine sample of 30%NiMnHCF; Figure S14: Pawley refinement of C1 of 30%NiMnHCF; Figure S15: Pawley refinement of D1 of 30%NiMnHCF; Figure S16: Pawley refinement of C2 of 30%NiMnHCF; Figure S17: Pawley refinement of D2 of 30%NiMnHCF; Figure S18: Pawley refinement of C10 of 30%NiMnHCF; Figure S19: Pawley refinement of C50 of 30%NiMnHCF; Figure S20: Pawley refinement of D50 of 30%NiMnHCF; Figure S21: Pawley refinement of C100 of 30%NiMnHCF; Figure S22: Pawley refinement of D100 of 30%NiMnHCF; Table S1: Performance of MnHCF cathode material in AZIBs; Table S2: List of samples analyzed with PXRD technique. References [44–46] are cited in the Supplementary Materials.

Author Contributions: Conceptualization, M.G. (Marco Giorgetti); methodology, M.G. (Marco Giorgetti), M.M. and G.A.; formal analysis, M.M.; investigation, M.M. and M.L.; resources, M.G. (Marco Giorgetti); data curation, M.M., M.L., I.C., M.G. (Mattia Gaboardi), G.A., J.R.P. and M.G. (Marco Giorgetti); writing—original draft preparation, M.M.; writing—review and editing, M.M., M.L. and M.G. (Marco Giorgetti); visualization, M.M.; supervision, M.G. (Marco Giorgetti); project administration, M.G. (Marco Giorgetti); funding acquisition, M.G. (Marco Giorgetti). All authors have read and agreed to the published version of the manuscript.

Funding: This research was funded by the Elettra synchrotron facility (2D-XRF, XANES measurements), #20220188; CERIC-ERIC, #20212162, #20222183 (PXRD measurement) (M.G. as PI); the RFO funds of the University of Bologna; MUR through the Sustainable Mobility Center, Centro Nazionale per la Mobilità Sostenibile—CNMS, Spoke 13 of the National Recovery and Resilience Plan (NRRP); the Ph.D. of M.M. was funded by the CERIC-ERIC.

Data Availability Statement: The raw data supporting the conclusions of this article will be made available by the authors on request.

Conflicts of Interest: The authors declare no conflicts of interest.

References

1. EUR-Lex. Available online: <https://eur-lex.europa.eu/summary/chapter/20.html#:~:text=The%20European%20climate%20law%20writes,2030,%20compared%20to%201990%20levels> (accessed on 23 February 2024).
2. Janssens, K.G. X-ray Fluorescence Analysis. In *Handbook of Spectroscopy*; Gauglitz, G., Vo-Dinh, T., Eds.; Wiley-VCH Verlag GmbH & Co. KGaA: Weinheim, Germany, 2003; Volume 11, pp. 363–419.
3. Maisuradze, M.; Carlomagno, I.; Mullaliu, A.; Li, M.; Aquilanti, G.; Giorgetti, M. 2D X-ray fluorescence imaging as a probe for charge state distribution of manganese in aged MnHCF-based electrodes. *J. Phys. Chem. C* **2023**, *127*, 21498. [[CrossRef](#)]
4. Booth, S.G.; Uehara, A.; Chang, S.Y.; Mosselmans, J.F.W.; Schroeder, S.L.M.; Dryfe, R.A.W. Gold Deposition at a Free-Standing Liquid/Liquid Interface: Evidence for the Formation of Au(I) by Microfocus X-ray Spectroscopy (μ XRF and μ XAFS) and Cyclic Voltammetry. *J. Phys. Chem. C* **2015**, *119*, 16785–16792. [[CrossRef](#)]
5. Yu, X.; Pan, H.; Zhou, Y.; Northrup, P.; Xiao, J.; Bak, S.; Liu, M.; Nam, K.-W.; Qu, D.; Liu, J.; et al. Direct Observation of the Redistribution of Sulfur and Polysulfides in Li–S Batteries During the First Cycle by In Situ X-Ray Fluorescence Microscopy. *Adv. Energy Mater.* **2015**, *5*, 1500072. [[CrossRef](#)]
6. Li, M.; Gaboardi, M.; Mullaliu, A.; Maisuradze, M.; Xue, X.; Aquilanti, G.; Plaisier, J.R.; Passerini, S.; Giorgetti, M. Influence of Vacancies in Manganese Hexacyanoferrate Cathode for Organic Na-ion Batteries: A Structural Perspective. *ChemSusChem* **2023**, *16*, e202300201. [[CrossRef](#)] [[PubMed](#)]
7. CATL. Available online: <https://www.catl.com/en/news/665.html> (accessed on 23 February 2024).
8. Altris. Available online: <https://www.altris.se/technology/> (accessed on 23 February 2024).
9. Natron Energy. Available online: <https://natron.energy/technology/> (accessed on 23 February 2024).

10. Fang, G.; Zhou, J.; Pan, A.; Liang, S. Recent Advances in Aqueous Zinc-Ion Batteries. *ACS Energy Lett.* **2018**, *3*, 2480–2501. [[CrossRef](#)]
11. Konarov, A.; Voronina, N.; Jo, J.H.; Bakenov, Z.; Sun, Y.-K.; Myung, S.-T. Present and Future Perspective on Electrode Materials for Rechargeable Zinc-Ion Batteries. *ACS Energy Lett.* **2018**, *3*, 2620–2640. [[CrossRef](#)]
12. Grignon, E.; Battaglia, A.M.; Schon, T.B.; Seferos, D.S. Aqueous Zinc Batteries: Design Principles toward Organic Cathodes for Grid Applications. *iScience* **2022**, *25*, 104204. [[CrossRef](#)] [[PubMed](#)]
13. Shibata, T.; Moritomo, Y. Ultrafast Cation Intercalation in Nanoporous Nickel Hexacyanoferrate. *Chem. Commun.* **2014**, *50*, 12941–12943. [[CrossRef](#)]
14. Takachi, M.; Fukuzumi, Y.; Moritomo, Y. Na⁺ Diffusion Kinetics in Nanoporous Metal-Hexacyanoferrates. *Dalton Trans.* **2016**, *45*, 458–461. [[CrossRef](#)]
15. You, Y.; Wu, X.-L.; Yin, Y.-X.; Guo, Y.-G. A Zero-Strain Insertion Cathode Material of Nickel Ferricyanide for Sodium-Ion Batteries. *J. Mater. Chem. A Mater.* **2013**, *1*, 14061. [[CrossRef](#)]
16. Qian, J.; Wu, C.; Cao, Y.; Ma, Z.; Huang, Y.; Ai, X.; Yang, H. Prussian Blue Cathode Materials for Sodium-Ion Batteries and Other Ion Batteries. *Adv. Energy Mater.* **2018**, *8*, 1702619. [[CrossRef](#)]
17. Wessells, C.D.; Peddada, S.V.; Huggins, R.A.; Cui, Y. Nickel Hexacyanoferrate Nanoparticle Electrodes for Aqueous Sodium and Potassium Ion Batteries. *Nano Lett.* **2011**, *11*, 5421–5425. [[CrossRef](#)] [[PubMed](#)]
18. Imanishi, N.; Morikawa, T.; Kondo, J.; Takeda, Y.; Yamamoto, O.; Kinugasa, N.; Yamagishi, T. Lithium Intercalation Behavior into Iron Cyanide Complex as Positive Electrode of Lithium Secondary Battery. *J. Power Sources* **1999**, *79*, 215–219. [[CrossRef](#)]
19. Eftekhari, A. Potassium Secondary Cell Based on Prussian Blue Cathode. *J. Power Sources* **2004**, *126*, 221–228. [[CrossRef](#)]
20. Wessells, C.D.; Huggins, R.A.; Cui, Y. Copper Hexacyanoferrate Battery Electrodes with Long Cycle Life and High Power. *Nat. Commun.* **2011**, *2*, 550. [[CrossRef](#)]
21. Wang, R.Y.; Shyam, B.; Stone, K.H.; Weker, J.N.; Pasta, M.; Lee, H.; Toney, M.F.; Cui, Y. Reversible Multivalent (Monovalent, Divalent, Trivalent) Ion Insertion in Open Framework Materials. *Adv. Energy Mater.* **2015**, *5*, 1401869. [[CrossRef](#)]
22. Mizuno, Y.; Okubo, M.; Hosono, E.; Kudo, T.; Ohishi, K.; Okazawa, A.; Kojima, N.; Kurono, R.; Nishimura, S.; Yamada, A. Electrochemical Mg²⁺ Intercalation into a Bimetallic CuFe Prussian Blue Analog in Aqueous Electrolytes. *J. Mater. Chem. A Mater.* **2013**, *1*, 13055. [[CrossRef](#)]
23. Park, H.; Lee, Y.; Ko, W.; Choi, M.; Ku, B.; Ahn, H.; Kim, J.; Kang, J.; Yoo, J.; Kim, J. Review on Cathode Materials for Sodium- and Potassium-Ion Batteries: Structural Design with Electrochemical Properties. *Batter. Supercaps* **2023**, *6*, e202200486. [[CrossRef](#)]
24. Li, M.; Maisuradze, M.; Sciacca, R.; Hasa, I.; Giorgiotti, M. A Structural Perspective on Prussian Blue Analogues for Aqueous Zinc-Ion Batteries. *Batter. Supercaps* **2023**, *6*, e202300340. [[CrossRef](#)]
25. Lu, Y.; Wang, L.; Cheng, J.; Goodenough, J.B. Prussian Blue: A New Framework of Electrode Materials for Sodium Batteries. *Chem. Commun.* **2012**, *48*, 6544. [[CrossRef](#)]
26. Mullaliu, A.; Asenbauer, J.; Aquilanti, G.; Passerini, S.; Giorgiotti, M. Highlighting the Reversible Manganese Electroactivity in Na-Rich Manganese Hexacyanoferrate Material for Li- and Na-Ion Storage. *Small Methods* **2020**, *4*, 1900529. [[CrossRef](#)]
27. Cao, T.; Zhang, F.; Chen, M.; Shao, T.; Li, Z.; Xu, Q.; Cheng, D.; Liu, H.; Xia, Y. Cubic Manganese Potassium Hexacyanoferrate Regulated by Controlling of the Water and Defects as a High-Capacity and Stable Cathode Material for Rechargeable Aqueous Zinc-Ion Batteries. *ACS Appl. Mater. Interfaces* **2021**, *13*, 26924–26935. [[CrossRef](#)]
28. Deng, W.; Li, Z.; Ye, Y.; Zhou, Z.; Li, Y.; Zhang, M.; Yuan, X.; Hu, J.; Zhao, W.; Huang, Z.; et al. Zn²⁺ Induced Phase Transformation of K₂MnFe(CN)₆ Boosts Highly Stable Zinc-Ion Storage. *Adv. Energy Mater.* **2021**, *11*, 2003639. [[CrossRef](#)]
29. Ni, G.; Hao, Z.; Zou, G.; Xu, X.; Hu, B.; Cao, F.; Zhou, C. Potassium Manganese Hexacyanoferrate with Improved Lifespan in Zn(CF₃SO₃)₂ Electrolyte for Aqueous Zinc-Ion Batteries. *Sustain. Energy Fuels* **2022**, *6*, 1353–1361. [[CrossRef](#)]
30. Fu, H.; Liu, C.; Zhang, C.; Ma, W.; Wang, K.; Li, Z.; Lu, X.; Cao, G. Enhanced Storage of Sodium Ions in Prussian Blue Cathode Material through Nickel Doping. *J. Mater. Chem. A Mater.* **2017**, *5*, 9604–9610. [[CrossRef](#)]
31. Yang, D.; Xu, J.; Liao, X.-Z.; He, Y.-S.; Liu, H.; Ma, Z.-F. Structure Optimization of Prussian Blue Analogue Cathode Materials for Advanced Sodium Ion Batteries. *Chem. Commun.* **2014**, *50*, 13377–13380. [[CrossRef](#)]
32. Maisuradze, M.; Li, M.; Aquilanti, G.; Plaisier, J.; Giorgiotti, M. Characterization of Partially Ni Substituted Manganese Hexacyanoferrate Cathode Material. *Mater. Lett.* **2023**, *330*, 133259. [[CrossRef](#)]
33. Lim, J.; Kasiri, G.; Sahu, R.; Schweinar, K.; Hengge, K.; Raabe, D.; La Mantia, F.; Scheu, C. Irreversible Structural Changes of Copper Hexacyanoferrate Used as a Cathode in Zn-Ion Batteries. *Chem. Eur. J.* **2020**, *26*, 4917–4922. [[CrossRef](#)] [[PubMed](#)]
34. Wang, K.; Guo, G.; Tan, X.; Zheng, L.; Zhang, H. Achieving high-energy and long-cycling aqueous zinc-metal batteries by highly reversible insertion mechanisms in Ti-substituted Na_{0.44}MnO₂ cathode. *J. Chem. Eng.* **2023**, *451*, 139059. [[CrossRef](#)]
35. Karydas, A.G.; Czyzycki, M.; Leani, J.J.; Migliori, A.; Osan, J.; Bogovac, M.; Wrobel, P.; Vakula, N.; Padilla-Alvarez, R.; Menk, R.H.; et al. An IAEA Multi-Technique X-Ray Spectrometry Endstation at Elettra Sincrotrone Trieste: Benchmarking Results and Interdisciplinary Applications. *J. Synchrotron. Radiat.* **2018**, *25*, 189–203. [[CrossRef](#)]
36. Jark, W.; Greici, G. Focusing X-Rays in Two Dimensions upon Refraction in an Inclined Prism. In Proceedings of the SPIE Optical Engineering + Applications, Advances in X-ray/EUV Optics and Components IX, San Diego, CA, USA, 17–21 August 2014; Volume 9207, p. 92070A. [[CrossRef](#)]
37. Solé, V.A.; Papillon, E.; Cotte, M.; Walter, P.; Susini, J. A Multiplatform Code for the Analysis of Energy-Dispersive X-ray Fluorescence Spectra. *Spectrochim. Acta Part B Spectrosc.* **2007**, *62*, 63–68. [[CrossRef](#)]

38. Ravel, B.; Newville, M. ATHENA, ARTEMIS, HEPHAESTUS: Data analysis for X-ray absorption spectroscopy using IFEFFIT. *J. Synchrotron Radiat.* **2005**, *12*, 537–541. [[CrossRef](#)] [[PubMed](#)]
39. Toby, B.H.; Von Dreele, R.B. GSAS-II: The genesis of a modern open-source all purpose crystallography software package. *J. Appl. Crystallogr.* **2013**, *46*, 544–549. [[CrossRef](#)]
40. Li, M.; Sciacca, R.; Maisuradze, M.; Aquilanti, G.; Plaisier, J.; Berrettoni, M.; Giorgetti, M. Electrochemical Performance of Manganese Hexacyanoferrate Cathode Material in Aqueous Zn-Ion Battery. *Electrochim. Acta* **2021**, *400*, 139414. [[CrossRef](#)]
41. Rodriguez-Hernández, J.; Reguera, E.; Lima, E.; Balmaseda, J.; Martínez-García, R.; Yee-Madeira, H. An Atypical Coordination in Hexacyanometallates: Structure and Properties of Hexagonal Zinc Phases. *J. Phys. Chem. Solids* **2007**, *68*, 1630–1642. [[CrossRef](#)]
42. Alfaruqi, M.H.; Mathew, V.; Gim, J.; Kim, S.; Song, J.; Baboo, J.P.; Choi, S.H.; Kim, J. Electrochemically Induced Structural Transformation in a γ -MnO₂ Cathode of a High Capacity Zinc-Ion Battery System. *Chem. Mater.* **2015**, *27*, 3609–3620. [[CrossRef](#)]
43. Huang, C.; Wu, C.; Zhang, Z.; Xie, Y.; Li, Y.; Yang, C.; Wang, H. Crystalline and Amorphous MnO₂ Cathodes with Open Framework Enable High-Performance Aqueous Zinc-Ion Batteries. *Front Mater. Sci.* **2021**, *15*, 202–215. [[CrossRef](#)]
44. Li, Q.; Ma, K.; Yang, G.; Wang, C. High-voltage non-aqueous Zn/K_{1.6}Mn_{1.2}Fe(CN)₆ batteries with zero capacity loss in extremely long working duration. *Energy Storage Mater.* **2020**, *29*, 246–253. [[CrossRef](#)]
45. Li, W.; Xu, C.; Zhang, X.; Xia, M.; Yang, Z.; Yan, H.; Yu, H.; Zhang, L.; Shu, W.; Shu, J. Sodium manganese hexacyanoferrate as Zn ion host toward aqueous energy storage. *J. Electroanal. Chem.* **2021**, *881*, 114968. [[CrossRef](#)]
46. Hou, Z.; Zhang, X.; Li, X.; Zhu, Y.; Liang, J.; Qian, Y. Surfactant widens the electrochemical window of an aqueous electrolyte for better rechargeable aqueous sodium/zinc battery. *J. Mater. Chem. A Mater.* **2017**, *5*, 730–738. [[CrossRef](#)]

Disclaimer/Publisher’s Note: The statements, opinions and data contained in all publications are solely those of the individual author(s) and contributor(s) and not of MDPI and/or the editor(s). MDPI and/or the editor(s) disclaim responsibility for any injury to people or property resulting from any ideas, methods, instructions or products referred to in the content.